TEMPLATE-FREE SYNTHESIS OF HOLLOW FE3O4 NANOPARTICLES AND THEIR APPLICATIONS IN LITHIUM-ION BATTERIES

A Thesis

Presented to the Faculty of the Graduate School

of Cornell University

In Partial Fulfillment of the Requirements for the Degree of

Master of Science

by

Zichao Yang

August 2009

ABSTRACT

The increase in the demand for power applications creates tremendous need to improve upon current lithium-ion battery technologies. The current work is concerned about the search for anode materials which are less prone to the pulverization problem and fast capacity fading. It has been proposed that hollow nanostructures are able to mitigate this problem and Fe_3O_4 is chosen as the subject of this study. Hollow Fe_3O_4 nanoparticles are synthesized via a template-free solvothermal method using $FeCl_3$ and urea as starting materials. Temporal XRD and TEM studies indicate that the growth follows an inside-out Ostwald ripening mechanism. Higher concentrations of urea in the starting material result in lower percentages of hollow particles and this observation is consistent with the proposed growth mechanism. The performance of the hollow particles as anode materials in lithium-ion batteries is tested and shown to be superior to their solid counterparts, with higher percentages of hollow particles giving better performance, which provides evidence for the hypothesis that hollow structures are able to alleviate the pulverization problem. Future work would mainly focus on the explicit substantiation of the hypothesis via post-mortem morphology and XRD studies and mechanical studies and other approaches to further improve the performance.

BIOGRAPHICAL SKETCH

Zichao Yang was born in Nov 1982 in Nanking, China and graduated from the National University of Singapore in 2004 with a Bachelor of Engineering (1^{st} Class Honors) in Chemical Engineering. After graduation, Zichao worked as a Research Officer for three years at the Institute of Bioengineering and Nanotechnology in Singapore. Zichao has been with the Chemical Engineering program at Cornell since 2007.

ACKNOWLEDGMENTS

I would like to express my gratefulness for all the guidance and support provided by my advisor, Professor Lynden Archer. I have gained a lot from discussions with and inspirations from Professor Archer. Comments from Professors Tobias Hanrath and Héctor Abruña are greatly appreciated. Thanks are also due to other group members for various help, to KAUST-Cornell Center for financial support and to Cornell Center for Materials Research for use of facilities.

TABLE OF CONTENTS

LIST OF TABLES

LIST OF FIGURES

INTRODUCTION

Lithium-ion batteries (LIBs) demonstrate higher energy density, higher operating voltage and lower self-discharge rates compared to conventional rechargeable batteries and have been widely employed in portable electronics applications. In recent years, the demand for rechargeable batteries with better performances is further increasing because of the development of hybrid and electric vehicles industry. Currently the most commonly used platform of electrode materials is graphite as the anode and $LiCoO_2$, $LiMn_2O_4$ or $LiNiO_2$ as the cathode. However, despite the intense research being performed worldwide, the performances achieved with these combinations are approaching their limits [1]. Therefore it is necessary to develop new classes of electrode materials with higher energy density and rate capability and better cycling performance.

The enhancement of the overall performance of LIBs will encompass various aspects including finding better materials for both the anode and the cathode, and improving on the properties of electrolytes, the recent increase in interest in the anode material has led the current work to focus on this area. The limited gravimetric capacity of graphitic carbon, which is the anode material used in the majority of current LIBs, has spurred tremendous interest and effort in research towards alternative anode materials with large capacities at low potentials. Unlike the conventional Li insertion/extraction process, these materials generally employ two types of mechanisms for Li storage: Li-metal alloying/dealloying (e.g. Si, Sn/SnO_2, Al, Sb) [2-4] and reversible formation-decomposition of Li_2O matrix for transition metal oxides (e.g. CoO, NiO, FeO) [5]. Transition-metal oxides have recently received much attention because of their high theoretical capacity (typically 2~3 times as high as 372 mAh/g for graphitic carbon). However, they are known to suffer from unsatisfactory cycling performance. This problem is partially attributed to the large volume changes and local stresses caused by

repeated Li^+ insertion and removal, resulting in breakdown of particles after many cycles (known as the pulverization problem), and to the growth of a polymer layer on the particles due to electrolyte degradation causing electrical isolation [5-7]. In the current work, attention will mainly be directed towards the former issue. The specific volume change for lithium insertion into SnO_2 and alloying with Sn is ~300% [2], and even the highly reversible conversion reactions are also associated with large volume changes, e.g. ~100% for $Co_3O_4 + 8Li \rightarrow 4Li_2O+3Co$ [4]. These volume changes induce stresses in the electrode material structure and during repeated cycles will cause fatigue in the materials and their eventual breakdown, loss of electric contact and loss of capacity. There are two main classes of approaches to mitigate/resolve the pulverization problem. One is to employ nanometer-scale particles with designed morphology, such as nanospheres, nanowires, nanotubes [8-14]. Among these, hollow nanoparticles (nanospheres) made of materials including SnO_2, Fe_2O_3, CuO and carbon have been investigated and shown to yield better performances [15-20] . For example, Wang *et al.* [13] prepared hollow SnO_2 nanotubes of ~200nm diameter and 10~25nm wall thickness by aggregation of SnO_2 nanoparticles in the size range of 6-15nm and found that the lithium storage capacity of the nanotubes is maintained at ~500mAh/g at 80 cycles, compared to <300mAh/g at 40 cycles. Lou *et al*. [19] synthesized hollow SnO_2 nanoparticles using a template-free approach and showed that their capacity is at ~500mAh/g at 50 cycles, compared to rapid fading in <20 cycles for pristine SnO_2 nanoparticles. The reason that hollow nano-/microstructures are able to perform better as LIB electrode materials has been proposed to include these factors [21]: a. the extra storage provided by the hollow space for Li^+ storage; b. larger surface area and shorter diffusion distance resulting in higher rate capabilities; c. higher mechanical flexibility due to the hollow structure, enhancing the ability of particles to maintain mechanical integrity.

Another approach is to use nanocomposite materials and an important example is the addition of carbon coatings on the nanoscale electrode material which can serve as a cushion and improve upon the electrical conductivity and cycling performance. The current work will first focus on the exploitation of hollow structures for the alleviation of the capacity fading problem by directly comparing the performances of hollow and solid particles in similar size ranges, with the aim of providing evidence for the hypothesis that hollow structures improves upon electrochemical performance because of its ability to buffer against volume change and mechanical stress. Following this, preliminary results on the carbon coating approach will be discussed.

Lithium-ion batteries are, in fact, only one area in which hollow nanomaterials are being employed and these materials are also finding applications in various other domains such as catalysis, sensing, photovoltaic cells, hydrogen storage and biomedical applications, due to their unique properties including large surface area and presence of hollow cavity. Previously, the most frequently used method of fabricating hollow nanoparticles has been template-based approach, namely, a template is first produced, followed by encapsulation by a shell material and elimination of the template, which may occur after or simultaneously with the attachment of shell layer. Different classes of materials/structures can serve as the template [21], for example, silica [22] or polymer nanoparticles [23] (hard template), metal nanoparticles [24] (sacrificial template) or micelles [25] / gas bubbles [26] (soft template). This platform of hollow particle synthesis has the advantage of being versatile in producing various types of hollow nanoparticles and being able to better control the particle size and cavity size, but is also associated with disadvantages such as tedious procedure and reduced quality because of the template removal step. In recent years, the template-free approach has drawn the attention of much research

mainly because of their simplicity and ease for potential scale-up. What is essential for the template-free approach is the hollowing process and the underlying reason for this process has frequently been attributed to be inside-out or "localized" Ostwald ripening, referring to the preferential dissolution of the particle interiors during the synthesis process. For instance, in the synthesis of Cu_2O hollow nanostructures [27], it was shown that the formation of such structure follows four steps: 1. generation of primary crystallites of CuO; 2. their aggregation to form larger particles; 3. reduction of CuO to Cu_2O; 4. inside-out Ostwald ripening to form the hollow cavities. The exact driving force and mechanism for the inside-out Ostwald ripening are still under investigation. For example, Yang *et al.* [28] reported a hydrothermal synthesis of hollow anatase TiO_2 nanoparticles from TiF_4 and the reduction of overall surface energy is hypothesized to be the driving force for the hollowing. The current work attempts to add to the understanding of this type of hollowing process based on the investigation of Fe_3O_4 system.

Magnetite (Fe_3O_4) is an important magnetic material and magnetite nanomaterials have found applications in diverse areas such as electronic devices, data storage, catalysis, drug delivery, medical diagnosis and so forth [29-34]. As a potential electrode material in LIBs, it has a theoretical capacity of 924 mAh/g, which is among the highest in transition metal oxides (see Table 1). It has the additional advantage of low cost and environmental benignity. Therefore it is chosen as the topic of the current study.

Magnetite has the formula Fe^{2+} $[Fe^{3+}{}_2]$ O_4 and adopts an inverse spinel structure. In each unit cell (containing 8 multiples of Fe_3O_4), 8 out of 16 Fe^{3+} ions occupy 8 out of the 64 tetrahedral sites and all the Fe^{2+} ions and the remaining 8 Fe^{3+} ions are distributed in 16 out of 32 octahedral sites. An early work has studied the use of Fe_3O_4

Material	Formula	Capacity (mAh/g)
Graphite	LiC_6	372 [2]
Lithium	Li	3862 [2]
Silicon	$Li_{4.4}Si$	4199 [35]
Tin oxide/tin	$Li_{21}Sn_5$	948 [2]
Cobalt oxide	$Co_3O_4 + 8Li^+$	890 [36]
Iron oxide	$Fe_3O_4 + 8Li^+$	924 [37]
Titanium oxide	$Li_{0.5}TiO_2$	167 [38]

Table 1: Comparison of theoretical capacities for several anode materials

as electrode materials in LIBs and based on XRD data and measured potentials vs. Li^+/Li for different lithiated iron oxides, Thackeray *et al.* [39] proposed that the lithiation of Fe_3O_4 follows the following pathway:

$$(Fe^{3+})[Fe_2^{3+/2+}]O_4 \xrightarrow{1.0\,Li} [Li^+Fe^{3+/2+}][Fe_2^{3+/2+}]O_4 \text{ (Phase 1)}$$

$$\xrightarrow{1.0\,Li} (Li^+)[Li^+Fe^{2+}][Fe_2^{2+}]O_4 \text{ (Phase 2)}$$

$$\xrightarrow{6.0\,Li} 4Li_2O + 3Fe \text{ (Phase 3)}$$

Here parentheses denote ions in tetrahedral sites and square brackets denote ions in octahedral sites. During the insertion of up to 1.0 Li, the Li^+ ions fill up octahedral vacancies, with Fe^{3+} in the tetrahedral sites displaced to octahedral sites, leading to the formation of a rock-salt-like structure of $Li_{1.0}Fe_3O_4$ at the end of this step. Further insertion of lithium involves the filling of the tetrahedral sites by Li^+ ions. Metallic iron is extruded from the rock-salt structure to accommodate the incoming Li^+ ions. More discussion on this process will follow in the results section with the analysis of cyclic voltammetry data.

In the recent years, the interest in the potential use of nanocrystalline magnetite as electrode materials in LIBs has been increasing. Thin films of nanocrystalline magnetite and magnetite-based composites have been studied [40, 41]. Mitra *et al.*

prepared Fe_3O_4 films on copper support via electrodeposition and determined the temperature and time conditions giving the best electrochemical performance. Sivakumar *et al.* [42] measured the change in magnetic properties of Fe_3O_4 upon lithiation and observed that change in magnetization chiefly occurred with the insertion of more than 1 mole of Li per formula unit. A few works have investigated the performance of Fe_3O_4 nanoparticles and the effect of various factors on their performance. Ito *et al.* [43] constructed a lithium battery using Fe_3O_4 particles of ~20nm size with India ink or polyvinyl alcohol additives and was able to achieve ~926 mAh/g capacity for three cycles at 60°C. Komaba *et al.* [44] and Zhu *et al.* [45] studied the correlation between crystallites size and performance and claimed that smaller grain sizes could result in higher capacities, although the mechanism was not clearly identified. Fe_3O_4 particles coated with materials such as carbon are also being investigated. Zhang *et al.* [46] and Liu *et al.* [47] synthesized carbon-coated Fe_3O_4 nanospindles and nanorods, respectively, which gave higher capacities and rate capabilities than uncoated Fe_3O_4.

The current work attempts to investigate the LIB performance of hollow Fe_3O_4 nanoparticles synthesized using a template-free approach. There have been a few reports on the template-free synthesis of hollow Fe_3O_4 nanoparticles. Chen *et al.* attempted to synthesize hollow Fe_3O_4 nanoparticles using a solvothermal approach and found that depending on the solvent and temperature being used, different products/morphologies can be obtained. Ethylene glycol as the solvent is able to yield Fe_3O_4 while water or ethanol leads to the formation of hematite or FeOOH. If water is used as the solvent, performing the reaction at 100°C and 180°C produced FeOOH nanorods and hematite polyhedrons respectively. Other workers have employed similar approaches but made use of slightly different starting materials [48-50]. Zhu *et*

al. heated a solution of $FeCl_3 \cdot 6H_2O$ and ethylenediamine in ethylene glycol to obtain hollow Fe_3O_4 nanoparticles or a mixture of hollow and solid particles. Guan *et al.* heated $[Fe(urea)_6]Cl_3$ in ethylene glycol and obtained a product which is at least partially hollow particles. In this work the method of Chen *et al.* is adapted to synthesize the hollow Fe_3O_4 nanoparticles.

In summary, the current work is aimed at determining the possible effect of employing hollow nanomaterials in enhancing the anode performances as compared to solid nanoparticles, using Fe_3O_4 as the model system.

MATERIALS AND METHODS

All chemicals were used as obtained without further purification. Fe_3O_4 nanoparticles were synthesized according to an approach similar to that reported by Chen *et al*.[51] 3mmol of $FeCl_3 \cdot 6H_2O$ (Mallinckrodt, 99.4%) and varying amounts of urea (Aldrich, 99.9%) were dissolved in 30mL of ethylene glycol (Aldrich, 99.8%) and heated at 200°C for up to 48hrs in a Teflon-lined stainless steel autoclave. The precipitates were separated by centrifugation, washed with absolute ethanol and dried at 80°C. For synthesis following the Zhu protocol, ethylenediamine (Aldrich, 99.5%) is used. The crystal structures of the particles were characterized using Scintag Theta-theta PAD-X X-Ray Diffractometer (Cu Kα,λ= 1.5406 Å) and their morphologies were studied using FEI Tecnai G2 T12 Spirit Transmission Electron Microscope (120kV).

The electrochemical properties of the hollow Fe_3O_4 nanoparticles as anode material in rechargeable lithium-ion batteries were measured at room temperature in homemade Swagelok-type cells. A picture of the cell used is shown in Figure 1.

Figure 1: Swagelok-type cells for electrochemical tests.

The working electrode consisted of 80 wt% of the active material (Fe_3O_4 nanoparticles), 10 wt% of carbon black (Super-P Li from TIMCAL) as a conductivity

aid, and 10 wt% of polymer binder (PVDF, polyvinylidene fluoride, Aldrich). To make the working electrode, a slurry containing the appropriate amounts of Fe_3O_4 active material (usually ~50mg), carbon black and a 2.5 wt% solution of PVDF in NMP (N-Methylpyrrolidone) is prepared and stirred overnight. The slurry is then applied onto a copper disk (0.007" thick, LYON industries) and the disk is dried in a vaccuum oven at 120°C for ~2hr. Lithium foil was used as the counter and reference electrodes. A 1 M solution of $LiPF_6$ in a 50:50 w/w mixture of ethylene carbonate and diethyl carbonate was used as the electrolyte. Celgard 2500 polypropylene membranes are used as the separator. Assembly of cell was performed in a glove box with moisture and oxygen concentrations below 1 ppm. The room-temperature electrode capacities were measured using Neware CT-3008 battery testers. Cyclic voltammetry measurements were carried out with an EDAQ EA161 Potentiostat on cells assembled using the same method as those used for capacity testing.

Preliminary nanoindentation tests were performed on a Veeco Dimension 3100 Ambient Atomic Force Microscope (AFM) using Veeco NP-10 silicon nitride probes with a nominal tip radius of 20nm. The sample is prepared by drop-casting a suspension of the nanoparticles in ethanol on a silicon substrate and drying it in air. The AFM tip gets into contact with the sample and applies a force on it, in an attempt to make an indentation. The force is proportional to the deflection (d) of the cantilever and the indentation depth is the difference between the deflection and the displacement of the pieso scanner (z). The tip approaches the sample and then retracts from it, from which two deflection-displacement plots are obtained. The elastic modulus is calculated using the Maugis model [52].

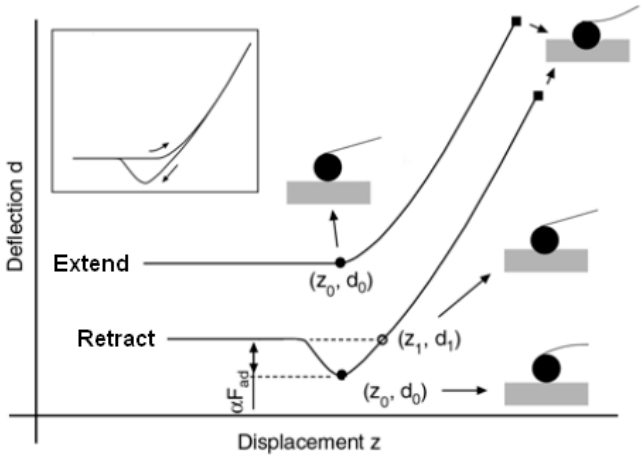

Figure 2: Deflection-displacement plots for extension and retraction. Picture from [53].

RESULTS AND DISCUSSION

Powder XRD patterns for reaction products obtained with phi=1.5 (here phi is defined as ratio of concentrations of urea and $FeCl_3$ in the starting material) at 6, 12, 24 and 48 hrs are shown in Figure 3. For 24 and 48 hrs, all peaks can be unequivocally indexed to represent the magnetite (Fe_3O_4) phase (JCPDS card no. 19-0629). For 6 and 12 hrs, the diffractograms indicate that the products are mixtures of different phases. The product for 12hrs (Fig. 2, with background subtracted) may contain Fe_3O_4, $Fe(OH)_3$ (JCPDS card no. 46-1436) and FeOOH (JCPDS card no. 34-1266). The 6hr product is similar to 12hr result except that the (311) peak for Fe_3O_4 is weak, indicating that there is still very little well-crystalline Fe_3O_4 phase formed at 6 hrs. From this analysis, a possible reaction mechanism for the formation of Fe_3O_4 may be proposed as follows:

$Fe^{3+} + 3OH^- \rightarrow Fe(OH)_3$ (OH^- from decomposition of urea)

$Fe(OH)_3 \rightarrow FeOOH + H_2O$

$Fe^{3+} \rightarrow Fe^{2+}$ (reduction by ethylene glycol)

$2Fe(OH)_3 + Fe^{2+} + 2OH^- \rightarrow Fe_3O_4 + 4H_2O$

$2FeOOH + Fe^{2+} + 2OH^- \rightarrow Fe_3O_4 + 2H_2O$

TEM pictures of the above products are shown in Figure 5. At 6 hrs, the product largely consists of small spindle-shaped particles (largely <50nm in length) with some large aggregates (a few hundred nm in size) formed from small particles. From the XRD analysis, these may be a mixture of $Fe(OH)_3$, FeOOH and possibly some fraction of amorphous Fe_3O_4. At 12hrs, the product is still a mixture of small particles and large aggregates, with more large aggregates seen. At 24 hrs and 48 hrs, the products consist of largely hollow Fe_3O_4 particles with some fractions

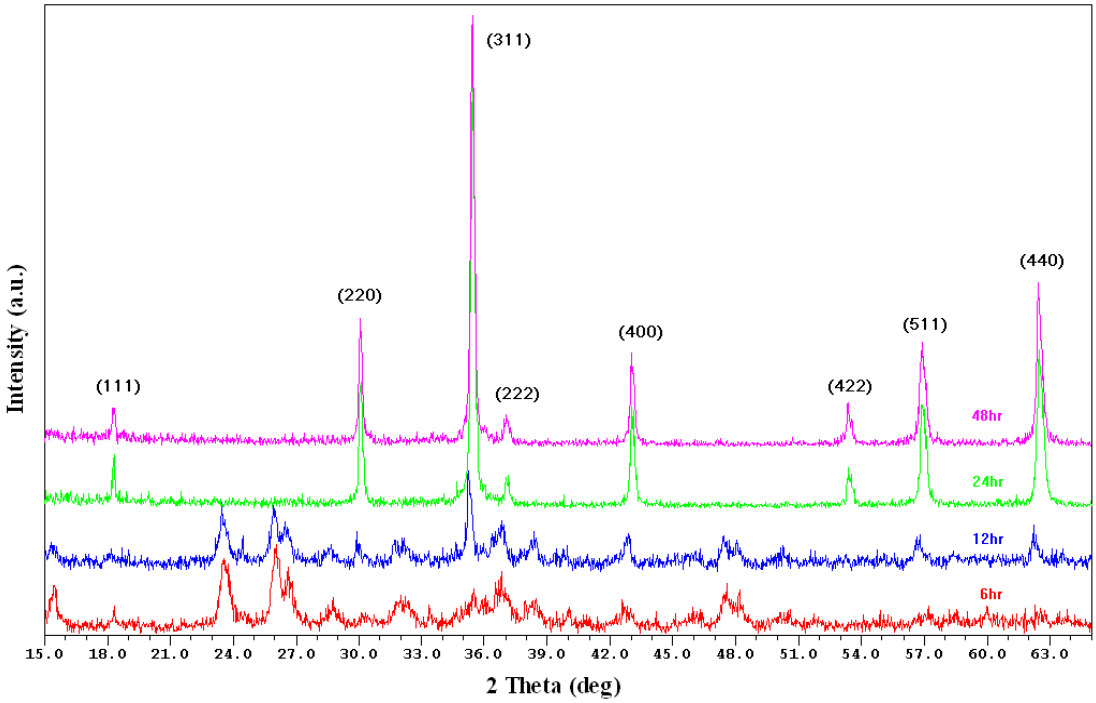

Figure 3: X-Ray Diffractograms of the Fe_3O_4 nanoparticles obtained with 1.5x urea

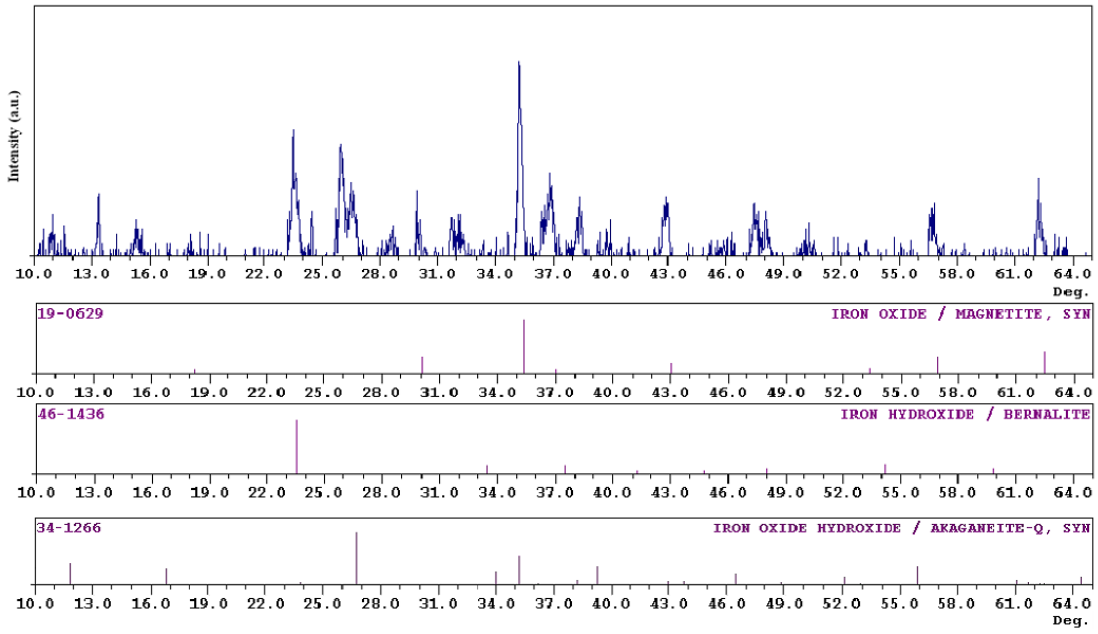

Figure 4: X-Ray Diffractograms of product at 12hr and for possible components

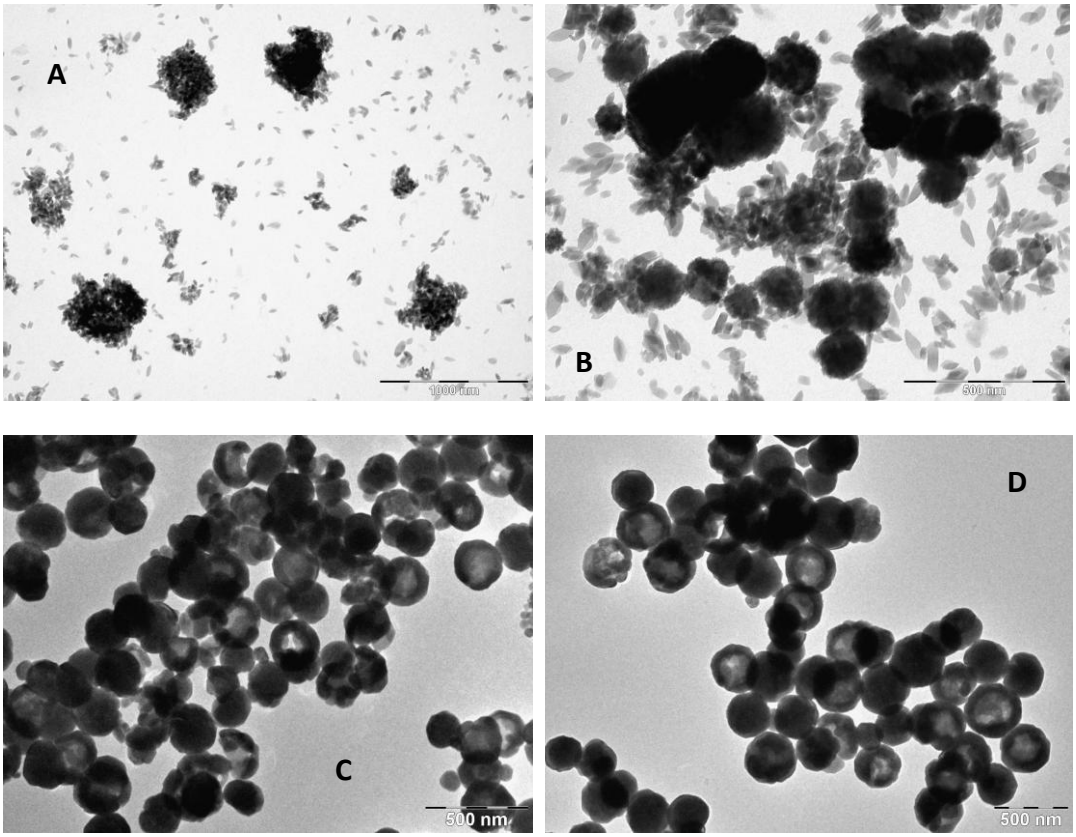

Figure 5: TEM pictures for products obtained with 1.5x urea at 6hr (A), 12hr (B), 24hr (C) and 48hr (D).

of solid Fe_3O_4 particles (particle size in the range of roughly 200~400nm). An analysis of the peaks in the XRD patterns using Scherrer equation shows the crystallite sizes for 6, 12, 24 and 48 hrs are approximately 39, 65, 96 and 97 nm, respectively, which is in agreement with what is shown in the TEM micrographs. Thus the growth process may be formulated as follows. The first phase is the formation of small particles (~50nm or smaller) following the reactions listed above, which then assemble into large particles (roughly 200~400nm in size). The driving force here may be the reduction of overall surface energy by forming aggregations. Then these bigger particles are transformed to hollow particles via inside-out Ostwald-ripening, during

which primary crystallites in the interior of the large particles preferentially dissolve and redeposit on the surface of large particles. The cause for the particles in the interior to be dissolved first is generally thought to be due to their higher surface energies [28]. However, no clear explanation has been provided so far as to why surface energies in the inside are higher. The reason could be that initially the large particles formed are only loose aggregates and as time proceeds, with the presence of some reactant species (especially OH^- in the case here) in the solution, smaller crystallites combine to form larger crystallites so that these large particles increase in crystallinity and are transformed to denser particles. The driving force for this process is the presence of reactants in the solution and because of the difficulty for the reactants to diffuse through the outer layers into the interior, the crystallization process in the interior may be slower, resulting in easier dissolution of the primary crystallites in the interior when Ostwald ripening which tends to minimized overall surface energy starts to occur. The overall process can be summarized in the schematic diagram below (Figure 6). This mechanism also explains why some solid particles are present in the final product as penetration of the particles by the solution takes time and not all particles will be able to start the core evacuation process.

It is found that changing experimental factors such as concentration of urea would affect the geometric features of the nanoparticles obtained. For a mixture of hollow and solid particles, the significant geometric features which could vary mainly include the average particle size, the percentage of hollow particles in the product, and the shell thickness of the hollow particles. An analysis of TEM pictures of the product is performed to extract such information. The method is as follows: choose areas on the TEM picture which contain mostly single layers of particles (i.e. not heavily aggregated with multiple layers of particles, since this makes counting of particles

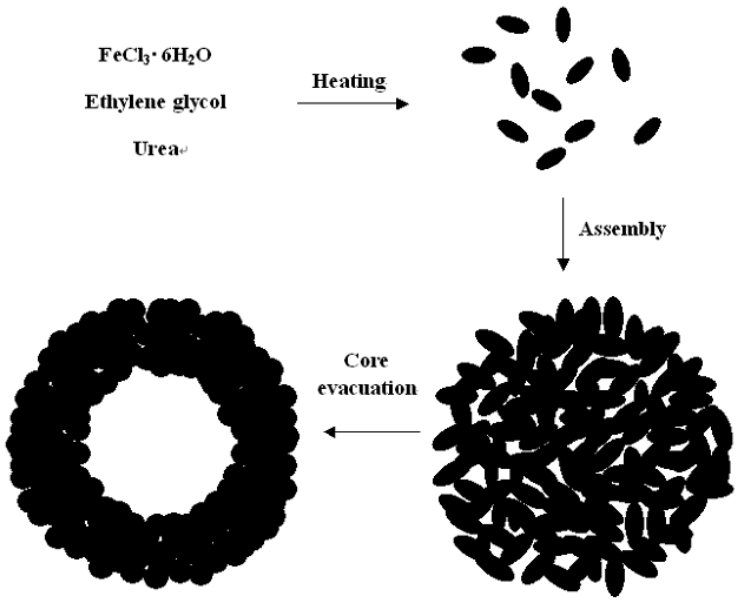

Figure 6: Schematic for formation of hollow nanoparticles.

difficult). Within such an area, a square of 2μm is drawn on the TEM picture at an arbitrary position and the sizes of all particles which lie fully within the square and whether they are hollow are recorded. Whether a particle should be counted as hollow sometimes can be ambiguous and the guideline here is that only when there is clear difference in contrast between the center region and the edge, the particle is counted as "hollow" and otherwise it is considered "solid", such that the percentage for hollow is not over-counted. Repeat this on a few pictures to obtain information about 50~100 particles, from which the average particle size and percentage hollow may be computed. Data on shell thickness can also be obtained, but this information is only able to give a rough idea on the "average" shell thickness as the sizes of particles for which the shell thickness is measured differ.

6x, 3x, 1.5x, 1.25x, and 1x (with respect to concentrations of iron precursor $FeCl_3$, i.e. 0.1M) of urea were added as the starting material to investigate the effect of urea concentration on the product. If no urea or less than ~0.5x of urea were used, no

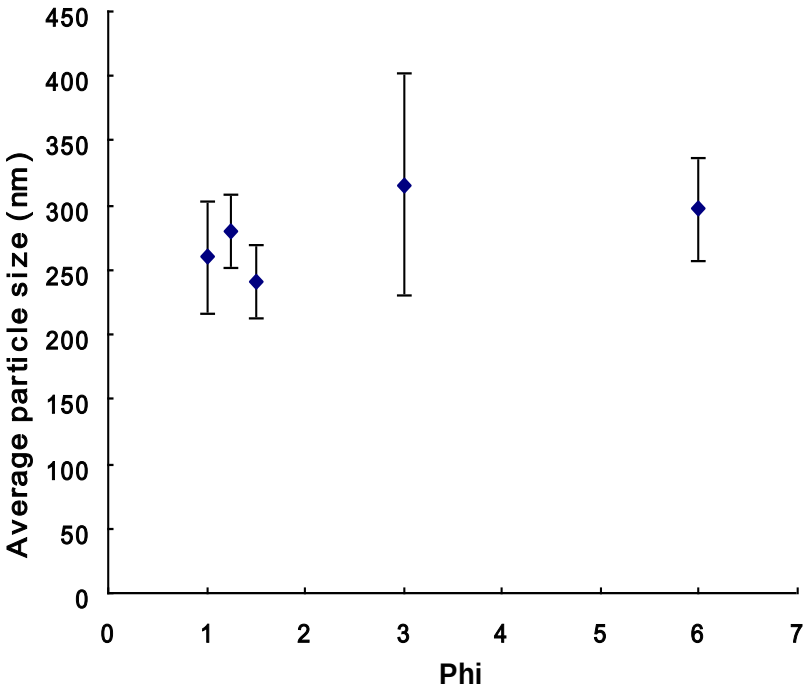

Figure 7: Particle size vs. Phi (Phi=[urea]/[Fe] in starting material)

appreciable amounts of well-crystalline Fe_3O_4 nanoparticles could be obtained. Data on the average particles size for these different batches of products are shown in Figure 7 (Phi=ratio of concentrations of urea to iron precursor).It is seen that for this synthesis protocol, the average size of particles is relatively close to 300nm and is not strongly affected by the ratio of concentration of urea to iron precursor. This fact would add more weight to the analysis of degree of hollowness of the product because if the sizes varied significantly for different phi values, the variation in size instead of variation in degree of hollowness could be the major effect of varying phi and it would be difficult to draw any conclusion for the observed difference in degree of hollowness.

The percentages of hollow particles are plotted versus the phi values in Figure 8:

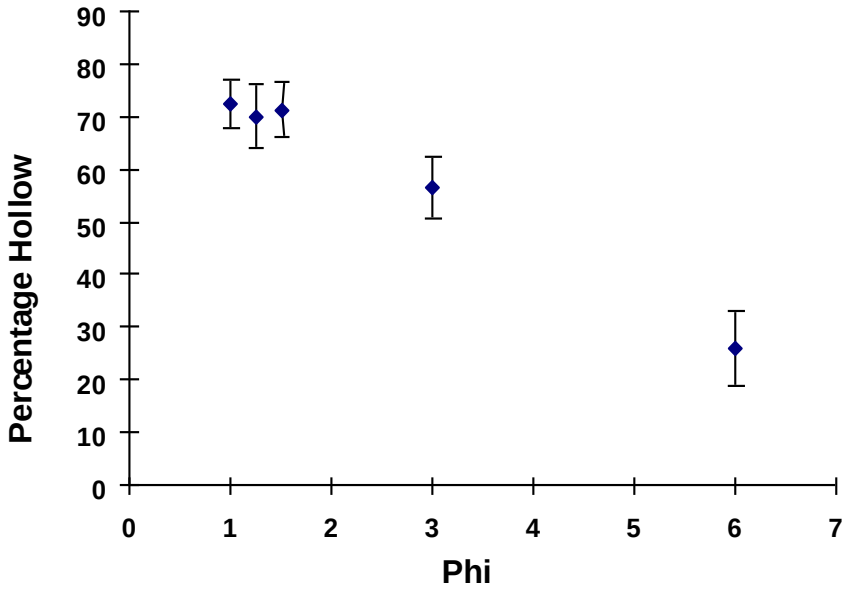

Figure 8: Percentage of hollow particles vs. Phi (Phi=[urea]/[Fe] in starting material)

The results indicate that lower amount of urea in the starting material would lead to larger percentage of hollow particles in the final product. This observation provides additional evidence for the inside-out Ostwald ripening mechanism of the formation of hollow spheres. As the hydroxyl ions released from decomposition of urea serve to facilitate the crystallization of the solid, higher concentrations of urea would imply that the particles are able to attain higher crystallinity in the same time frame. Thus the process of the dissolution and evacuation of the particle interior would be more difficult, resulting in lower percentages of hollow particles with other conditions being the same. However, if the urea concentration is reduced to less than ~0.5x, well-crystalline Fe_3O_4 nanoparticles could not be obtained probably because the reaction is unable to proceed in the manner proposed above due to lack of reactant.

The performance of the hollow Fe_3O_4 nanoparticles as anode material in lithium-ion batteries was tested. Cyclic voltammograms for the first four cycles at a scan rate of

0.2mV/s are shown in Figure 9. In the first cycle, the large peak at 0.49V in the cathodic scan may be attributed to the reduction of Fe_3O_4 to Fe with formation of Li_2O. This reduction process was proposed to be broken up into different phases as described in the introduction, which can be verified by the data for the following cycles. It is seen that peaks 1 and 4 may correspond to stage 2, namely, the reduction of $LiFe_3O_4$ to $Li_2Fe_3O_4$, noting that all the Fe^{3+} ions are now reduced to Fe^{2+}, and the corresponding oxidation process, respectively. Peaks 2 and 3 then may correspond to stage 3, the reduction of Fe^{2+} to Fe^0, and the corresponding oxidation process, respectively. However, in the first cycle, the proposed different stages appear to show up as only one big peak. This would indicate that the forms of the electrode material differ at the start of the first cycle and at the start of the following cycles. The proposed 1st step, namely, the insertion of up to 1 Li, is irreversible because of the kinetic barrier on the extraction of Li from the rock salt structure [54]. Therefore it is likely that the following cycles will start with $LiFe_3O_4$. The reason that the reduction occurs at lower voltages than the following cycles could also be attributed to the presence of a kinetic barrier for the insertion of up to 1 Li which creates an overpotential which shifts all the following reactions towards lower voltages. These reactions corresponding to different stages can hardly be differentiated as distinct peaks because their voltages are too close to each other (in fact a small kink can still be observed at ~0.70V).

In addition to the analysis so far, a closer look at the change of peaks with the increase of cycle number reveals more information about the process. The potential for peak 2 appears to shift towards lower voltages along with the increase of cycle number (from 0.85V to 0.82V from cycle 2 to cycle 4). For peak 3 it might be somewhat ambiguous to exactly define where the peak is but they all appear to be very close to 1.75V. Thus,

there is an increase in the separation of peak potentials E_{pa}-E_{pc}, which indicates a decrease in the reversibility of the reaction along the cycles [55]. The change in reversibility of the reaction is of interest because this correlates with the decrease in charge/discharge capacity in LIBs. As the irreversibility of the reaction increases, the Coulombic efficiency decreases and the fraction of Li inserted in the previous cycle which cannot be extracted during the following cycle increases, resulting in reduction of capacity. Another factor to be considered is the ratio of peak currents (i_{pa}/i_{pc}, i.e. i_{peak3}/i_{peak2}), changing from 0.56 (cycle 2) to 0.42 (cycle 4), a 1.34-fold increase in deviation from 1, which also substantiates conclusion of increasing irreversibility. Whereas for peaks 1 and 4, E_{pc} shifts from 1.20V (cycle 2) to 1.23V (cycle 4) and E_{pa} all appears to be very close to 1.93V. i_{pa}/i_{pc} changes from 1.10 (cycle 2) to 1.45 (cycle 4), a 1.31-fold increase in deviation from 1. From these numerical results, it is seen that reaction corresponding to peaks 2 and 3 (i.e. reduction of Fe^{2+} to Fe^{0}), has a tendency to increase faster in terms of irreversibility, as compared to reaction corresponding to peaks 1 and 4 (i.e. reduction of Fe^{3+} to Fe^{2+}). Thus it can be concluded that reduction reaction of Fe^{2+} to Fe^{0} may be the strongest contributor to the fading of charge/discharge capacity (except the first cycle).

Figure 10 shows typical discharge and charge curves for 1^{st}, 2^{nd} and 55^{th} cycles obtained at 200mA/g (~0.25C) with a voltage window of 5mV~3V. The first discharge curve has a plateau at ~0.8V and shifts to slightly more positive potentials in the following cycles, which is consistent with results described in the literature [40, 41] and roughly corresponds to the trend observed in the cathodic scan of CV. Leftward shift of the curves indicate reduction in capacity.

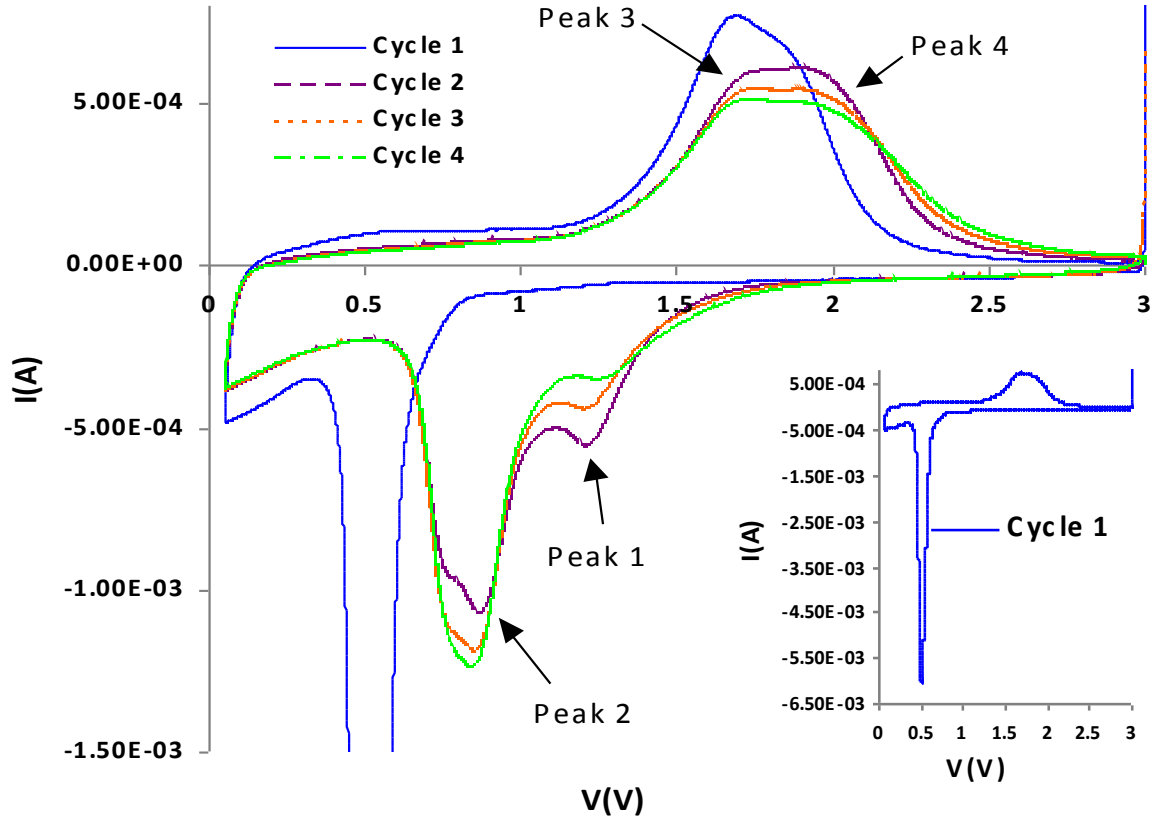

Figure 9: Cyclic voltammograms of hollow Fe_3O_4 nanoparticles for cycles 1 to 4. Inset: CV for cycle 1.

To compare the performance of hollow versus solid Fe_3O_4 nanoparticles, the cycling performances of hollow particles produced with different concentrations of urea (Phi=1, 3) as the starting material were measured, together with that of solid Fe_3O_4 nanoparticles (particle size 192±44nm, synthesized according to a method similar to that used by Zhu *et al.* [49]. Refer to TEM image in Figure 11).

The Coulombic efficiency with respect to cycle number is plotted in Figure 12 (left axis) and it is seen that in the first few cycles and in the following cycles, the reversibility of phi=1 (~70% hollow) is the highest, followed by phi=3 (~55% hollow)

and that of the solid particles appears to the lowest, indicating the sample with a higher fraction of hollow particles is more able to withstand the tendency to lose reversibility. Charging capacities with respect to cycle number are shown in Figure 12 (right axis). The capacity for solid particles starts at a value of ~760mAh/g and fades relatively quickly (to about half of initial value at ~20 cycles). For phi=1 and phi=3 samples, higher fraction of hollow particles corresponds to higher capacity and slower capacity fading. This observation is consistent with the hypothesis that hollow nanoparticles yield better capacity and cycling performance compared to their solid counter parts of roughly comparable size. A number of previous reports have compared hollow particles on the scale of hundreds of nanometers and solid particles on the scale of 10nm [13, 17, 19] and it would be more insightful to compare hollow and solid particles on the same size scale, as Li *et al.* [56] did for nanotubes, nanorods and nanoparticles which are all in the hundreds of nm range. It should be admitted that there is still difference in the sizes of samples compared here and it would be more conclusive to use samples which have narrower size distributions and even closer sizes. This point is further discussed under “synthesis approach” in the Future Work section.

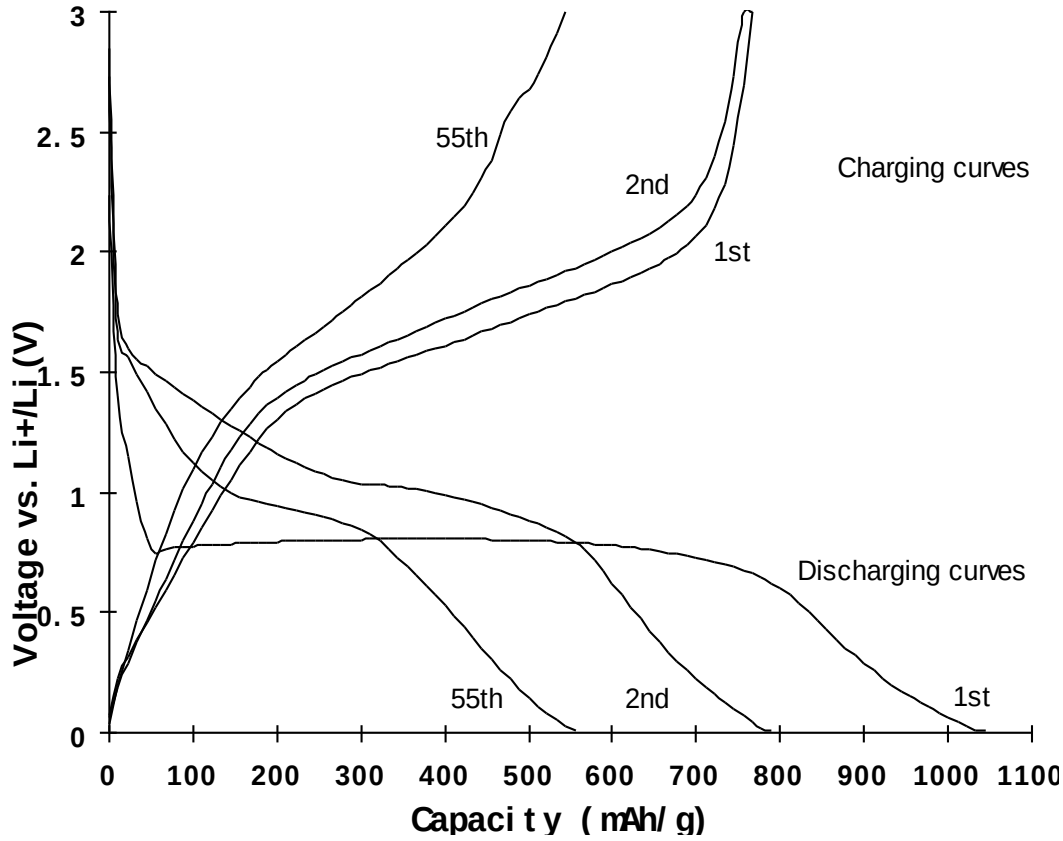

Figure 10: Voltage vs. capacity curves for cycles 1, 2 and 55 for phi=1.

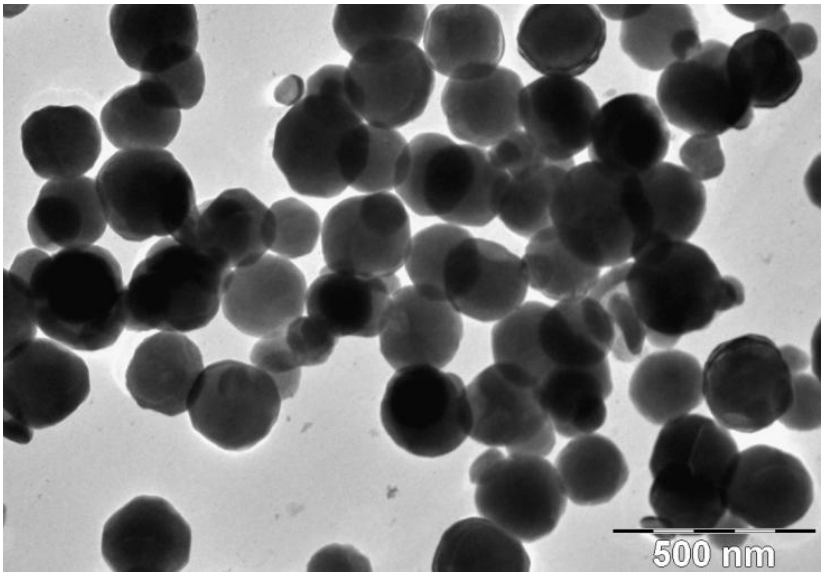

Figure 11: Sample TEM picture for solid nanoparticles.

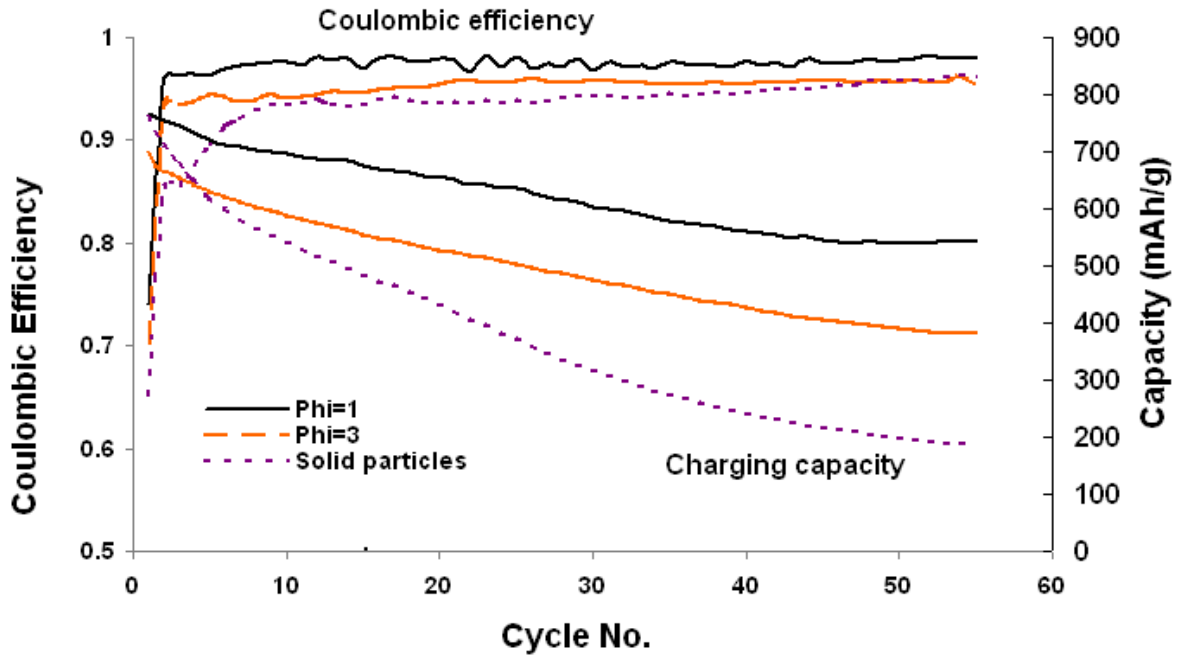

Figure 12: Coulombic efficiency and Charging capacity with respect to cycle number for Phi=1,3 and solid particles at 200mA/g charge/discharge rate.

FUTURE WORK

1. Post-mortem morphology studies

As has been mentioned earlier, one of the main hypotheses of this work is that the hollow nanostructures are able to give better cycling performance than the solid counterparts because of their higher mechanical flexibility and the ability of the internal void to buffer against the large volume changes during lithium insertion/extraction [13, 14, 17, 18, 57]. However, there have been few post-mortem studies on these hollow structures to investigate what actual transformation they undergo and what is the morphology of the particles at the end of the cycling. Such information would provide a basis for comparison of the abilities of hollow and solid nanoparticles to withstand volume changes and tendency to pulverize. In addition post-mortem studies may also provide information on growth of SEI films which will help in the understanding of effect of coatings. Therefore, future work would include comparative TEM studies of hollow and solid nanoparticles. Specifically, after the same number of cycles, the active material particles will be collected and investigated under TEM and an analysis of relative numbers of intact/broken particles will be performed and the result will be correlated with the electrochemical performance recorded. XRD studies will also be carried out on these intermediate products as a way of obtaining extra information on the potential changes in crystallinity which occur to the active materials during cycling.

Sample post-mortem TEM analysis has been carried out on hollow SnO_2 nanoparticles (synthesized according to [19]) and morphologies of the end product of the electrode material after the cell has failed were observed (Figure 13). The material was removed from the copper electrode, washed carefully with chloroform to remove the binder (polyvinylidene difluoride) and was then observed under TEM. For comparison,

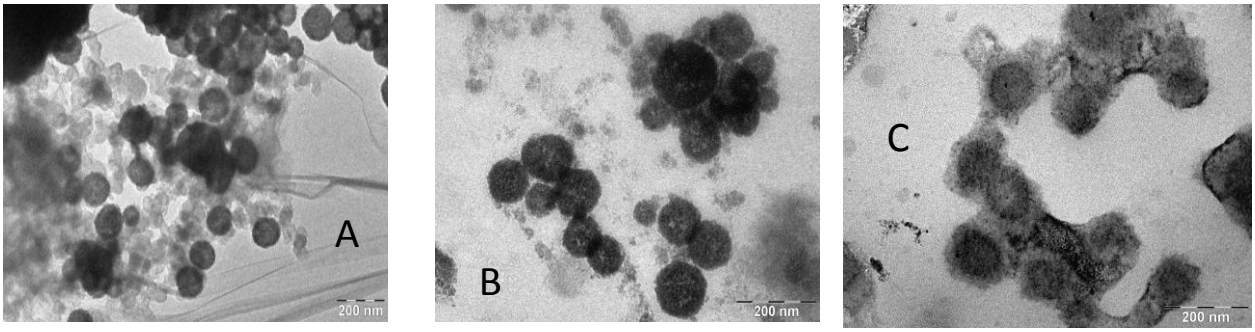

Figure 13: TEM pictures for electrode material (SnO_2/C) before (A) and after (B and C) testing.

pictures of the mixture of active material with carbon black (conductivity aid) before the test were also taken. By comparing these pictures, it is seen that depending on the runs, the nanoparticles can either still be maintaining their shape or can have started to undergo changes in structure by the end of the test. In fact both types may exist in the same sample. Thus it is not clear at this stage whether hollow particles are able to maintain their structures during the cycles. To elucidate this, the counting of hollow particles and correlation with electrochemical performance will be carried out.

2. Study of mechanical properties

Another aspect in understanding the advantages of using hollow structures is to measure the mechanical strengths of hollow nanoparticles as compared to solid nanoparticles. A useful tool for this study is nanoindentation which yields information on elastic modulus of the sample. Particles with different thicknesses will be indented and their moduli measured, which provides information on strength of the particles and can then be correlated with the electrochemical performance. For such correlation to be reliable, it would be more desirable to perform the test on particles with more uniform size distribution, which is discussed below in “synthesis approach”.

A preliminary run was done on the hollow nanoparticles and the following result was obtained.

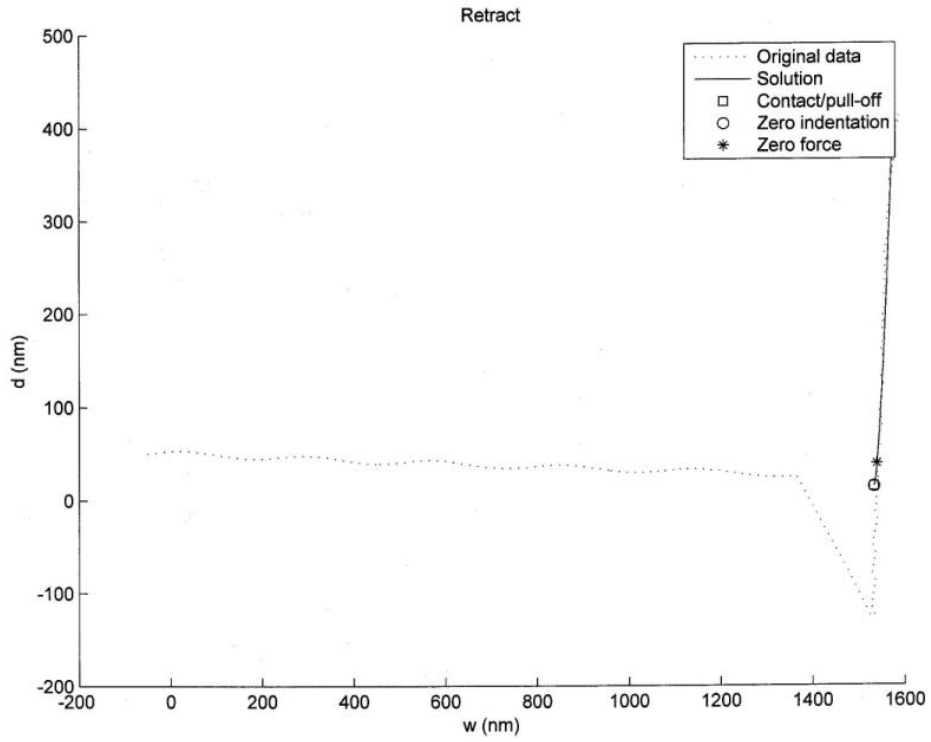

Figure 14: Deflection-displacement curve for retraction

Model fitting of the data yields E=9.81MPa. The elastic modulus of bulk magnetite is 242 GPa [58]. The obtained result is clearly significantly below the expect range and much lower than the elastic modulus for the silicon substrate (~150 GPa) as well. The reason could lie in the fact that while the hollow particle is placed on the substrate, it is likely to shift when getting into contact with the AFM tip. The measured displacement would thus be much larger than the any actual indention, leading to a shrunk modulus result. However, it should be noted that even if the hollow particle is firmly linked to the substrate surface, the measured displacement is still in fact a combined result of indentation plus the displacement caused by the buckling of the

hollow particle. Thus the real indentation may not be able to be accurately extracted. What may need to be done is to employ a blunt-tip which together with the substrate squeezes the particle and the displacement would mainly be caused by the buckling deformation, from which the mechanical strength could be computed.

3. Carbon coating

Transition-metal oxide materials have limited electrical conductivity and it has often been proposed that coatings inceasing conductivity be added to these materials so that better rate capability and can be improved. In the mean time, these coatings may also serve to provide extra support and thus enhance the mechanical stability of the particles, leading to improved capacities. Examples include porous SnO_2 nanotubes with coaxially grown carbon nanotube overlayers [14], hollow SnO_2 nanoparticles synthesized using a template-free approach and coated with amorphous carbon [59], magnetite nanospindles [46] and nanorods [47] with carbon coatings. The carbon coatings could be in the form of amorphous carbon or graphitic carbon depending on the precursor used for carbon formation.

Preliminary experiments have been carried out on coating the hollow Fe_3O_4 nanoparticles using polysaccharides as the precursor. The experimental procedure is similar to that described in [46]. Hollow Fe_3O_4 nanoparticles are suspended in a mixture of ethanol and water with a certain amount of glucose added and the mixture is sealed in a Teflon-lined stainless steel autoclave and heated at 150°C. The product is then separated from the mixture, washed and dried. A sample TEM picture is shown in Figure 15. Although more thorough TEM characterization is needed, this picture indicates the presence of carbon-like phases (the honeycomb-like area in the picture). The electrochemical performance of this carbon-composited material is shown in

Figure 16. The increase of capacity with respect to cycle number is a relatively rare and very interesting phenomenon and understanding the mechanism behind this observation is likely to shed light on how to design the carbon coating process to improve upon the performance. Decomposition of glucose alone (without Fe_3O_4) under the same conditions produces a black carbon-like material and electrochemical tests show that such material has very little Li^+ storage capacity, indicating that the gradual capacity increase is not due to the presence of carbon itself. The increase of capacity with respect to cycle number has been reported before [6, 60]. This increase is proposed to be due to the formation of Li_2O in the first cycle which could not be reversibly converted back to Li in the early stages. As the cycle number increases, some type of rearrangement of electrode material is thought to occur which recovers the reversible capacity. This mechanism is not yet able to explain why the increase in only observed in the carbon-composited Fe_3O_4 but not in the original Fe_3O_4 nanoparticles. Other hypotheses can be made and this increase could be because the polysaccharide (glucose) reacted with the surface layers of the Fe_3O_4 nanoparticles causing a change in composition in only these surface layers. These layers with a new composition may have a relatively low electrochemical capacity compared to the internal layers which may have retained their original composition. Because the lithium ions need to diffuse into the interior of the particles to utilize the capacity there, as the cycle number increases, some material in the interior of the particles may become more accessible for Li^+ storage (possibly because of some rearrangement mechanism), thus resulting in increased capacity. To verify this hypothesis, XRD analysis need to be performed on the material and EDX studies need to be carried out on different parts of the material to determine any differences in composition. Cyclic voltammetry may also be used to study change in potentials at which electrochemical reactions occur for the new material.

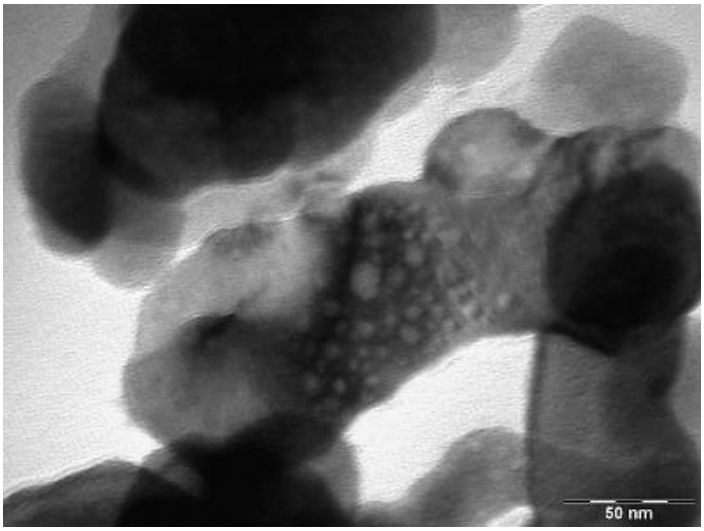

Figure 15: Sample TEM picture for carbon-composited Fe_3O_4

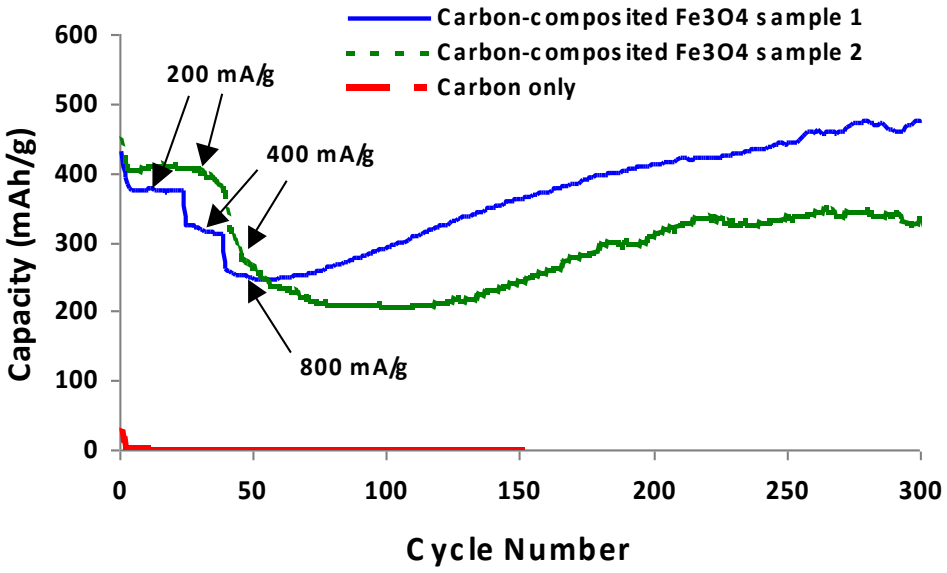

Figure 16: Electrochemical performance of carbon-composited Fe_3O_4 nanoparticles

4. Synthesis approach

The materials obtained using template-free solvothermal synthesis method generally have the problem of relatively high polydispersity. Although higher polydispersity is not necessarily associated with reduced performance, it makes the analysis of the results more difficult. In [51], it is proposed that adding polyvinylpyrrilidone (PVP) as a starting material would lead to more uniformly sized product. The approach has been attempted for phi=1.5 and a sample TEM is shown in Figure 17. Analysis of the TEM pictures yields a particle size distribution of 298±77nm and a hollow percentage of 64.7±3.8%. Compared to 241±28nm and 71.3±5.2% hollow for the case where no PVP is added, it cannot be concluded that PVP will improve on the size distribution or increase the percentage hollow. Thus, other approaches need to be sought.

Template-based approaches (e.g. hard template) are known to yield better size distributions [21]. Although not explicitly studied, hollow nanoparticles material synthesized using template-based approach (with more uniform size distribution) may show better performance than those made using the template-based approach in some cases [59, 61]. Therefore, an aspect of the future work would be to employ template based approach to synthesize hollow nanoparticles with more uniform size distribution. Silica synthesized using the Stöber method is a candidate for the template [61].

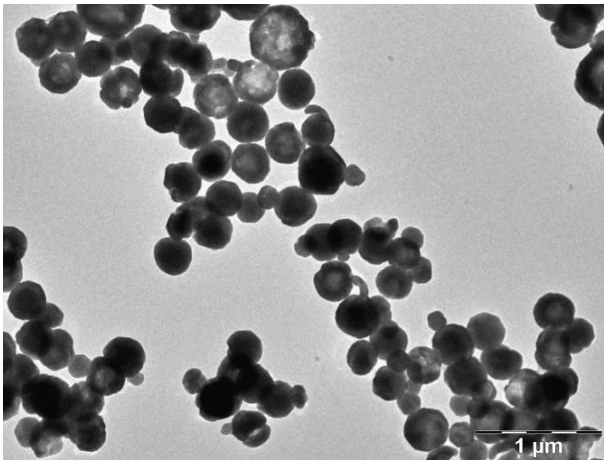

Figure 17: Sample TEM picture for particles synthesized with the presence of PVP.

CONCLUSION

In conclusion, hollow Fe_3O_4 nanoparticles were synthesized using a template-free approach. Temporal XRD and TEM studies indicate that the growth follows an inside-out Ostwald-ripening process. The concentration of one of the reactants, urea, was shown to have a significant effect over the fraction of hollow particles in the product, with higher urea concentration (not lower than ~0.5x) leading to lower percentage of hollow particles. This observation is in agreement with the Ostwald ripening mechanism for the hollowing process because urea aids in the crystallization of the product and higher urea concentration causes the dissolution and hollowing of the particle interior to become more difficult. Results on the electrochemical performance of the particles as anode material in lithium-ion batteries show that the hollow nanoparticles exhibit higher capacities than their solid counterparts with comparable size, which provides evidence for the hypothesis that hollow structures have the advantage of being able to alleviate the pulverization problem.

Future work mainly includes post-mortem morphology and XRD studies and mechanical studies on hollow Fe_3O_4 nanoparticles, carbon coating on these hollow Fe_3O_4 nanoparticles for the improvement of electrochemical performance and synthesis of hollow Fe_3O_4 nanoparticles by template-based approach.

REFERENCES

1. Tarascon, J.M. and M. Armand, *Issues and challenges facing rechargeable lithium batteries.* Nature, 2001. **414**(6861): p. 359-367.
2. Winter, M., et al., *Insertion electrode materials for rechargeable lithium batteries.* Advanced Materials, 1998. **10**(10): p. 725-763.
3. Tirado, J.L., *Inorganic materials for the negative electrode of lithium-ion batteries: state-of-the-art and future prospects.* Materials Science & Engineering R-Reports, 2003. **40**(3): p. 103-136.
4. Larcher, D., et al., *Recent findings and prospects in the field of pure metals as negative electrodes for Li-ion batteries.* Journal of Materials Chemistry, 2007. **17**(36): p. 3759-3772.
5. Poizot, P., et al., *Nano-sized transition-metaloxides as negative-electrode materials for lithium-ion batteries.* Nature, 2000. **407**(6803): p. 496-499.
6. Grugeon, S., et al., *An update on the reactivity of nanoparticles Co-based compounds towards Li.* Solid State Sciences, 2003. **5**(6): p. 895-904.
7. Dedryvere, R., et al., *Contribution of X-ray photoelectron spectroscopy to the study of the electrochemical reactivity of CoO toward lithium.* Chemistry of Materials, 2004. **16**(6): p. 1056-1061.
8. Park, M.S., et al., *Preparation and electrochemical properties of SnO2 nanowires for application in lithium-ion batteries.* Angewandte Chemie-International Edition, 2007. **46**(5): p. 750-753.
9. Yuan, Z.Y., et al., *Synthesis and electrochemical performance of nanosized Co3O4.* Materials Chemistry and Physics, 2003. **79**(1): p. 1-4.
10. Larcher, D., et al., *The electrochemical reduction of Co3O4 in a lithium cell.* J. Electrochem. Soc., 2002. **149**(3): p. A234-A241.

11. Li, Y.G., B. Tan, and Y.Y. Wu, *Mesoporous CO3O4 nanowire arrays for lithium ion batteries with high capacity and rate capability.* Nano Letters, 2008. **8**(1): p. 265-270.

12. Zhou, Y.K., et al., *Lithium insertion into TiO2 nanotube prepared by the hydrothermal process.* Journal of the Electrochemical Society, 2003. **150**(9): p. A1246-A1249.

13. Wang, Y., J.Y. Lee, and H.C. Zeng, *Polycrystalline SnO2 nanotubes prepared via infiltration casting of nanocrystallites and their electrochemical application.* Chemistry of Materials, 2005. **17**(15): p. 3899-3903.

14. Wang, Y., H.C. Zeng, and J.Y. Lee, *Highly reversible lithium storage in porous SnO2 nanotubes with coaxially grown carbon nanotube overlayers.* Advanced Materials, 2006. **18**(5): p. 645-+.

15. Zeng, S.Y., et al., *Hematite hollow spindles and microspheres: Selective synthesis, growth mechanisms, and application in lithium ion battery and water treatment.* Journal of Physical Chemistry C, 2007. **111**(28): p. 10217-10225.

16. Park, J.C., et al., *Gram-Scale Synthesis of Cu2O Nanocubes and Subsequent Oxidation to CuO Hollow Nanostructures for Lithium-Ion Battery Anode Materials.* Advanced Materials, 2009. **21**(7): p. 803-+.

17. Han, S.J., et al., *Simple synthesis of hollow tin dioxide microspheres and their application to lithium-ion battery anodes.* Advanced Functional Materials, 2005. **15**(11): p. 1845-1850.

18. Wang, Y., et al., *Crystalline carbon hollow spheres, crystalline carbon-SnO2 hollow spheres, and crystalline SnO2 hollow spheres: Synthesis and performance in reversible Li-ion storage.* Chemistry of Materials, 2006. **18**(5): p. 1347-1353.

19. Lou, X.W., et al., *Template-free synthesis of SnO2 hollow nanostructures with high lithium storage capacity.* Advanced Materials, 2006. **18**(17): p. 2325-+.

20. Deng, D. and J.Y. Lee, *Hollow core-shell mesospheres of crystalline SnO2 nanoparticle aggregates for high capacity Li+ ion storage.* Chemistry of Materials, 2008. **20**(5): p. 1841-1846.

21. Lou, X.W., L.A. Archer, and Z.C. Yang, *Hollow Micro-/Nanostructures: Synthesis and Applications.* Advanced Materials, 2008. **20**(21): p. 3987-4019.

22. Zhong, Z.Y., et al., *Preparation of mesoscale hollow spheres of TiO2 and SnO2 by templating against crystalline arrays of polystyrene beads.* Advanced Materials, 2000. **12**(3): p. 206-+.

23. Caruso, F., R.A. Caruso, and H. Mohwald, *Nanoengineering of inorganic and hybrid hollow spheres by colloidal templating.* Science, 1998. **282**(5391): p. 1111-1114.

24. Liang, H.P., et al., *Pt hollow nanospheres: Facile synthesis and enhanced electrocatalysts.* Angewandte Chemie-International Edition, 2004. **43**(12): p. 1540-1543.

25. Zoldesi, C.I. and A. Imhof, *Synthesis of monodisperse colloidal spheres, capsules, and microballoons by emulsion templating.* Advanced Materials, 2005. **17**(7): p. 924-+.

26. Peng, Q., Y.J. Dong, and Y.D. Li, *ZnSe semiconductor hollow microspheres.* Angewandte Chemie-International Edition, 2003. **42**(26): p. 3027-3030.

27. Teo, J.J., Y. Chang, and H.C. Zeng, *Fabrications of hollow nanocubes of Cu2O and Cu via reductive self-assembly of CuO nanocrystals.* Langmuir, 2006. **22**(17): p. 7369-7377.

28. Yang, H.G. and H.C. Zeng, *Preparation of hollow anatase TiO2 nanospheres via Ostwald ripening.* Journal of Physical Chemistry B, 2004. **108**(11): p. 3492-3495.

29. Jeong, U., et al., *Superparamagnetic colloids: Controlled synthesis and niche applications.* Advanced Materials, 2007. **19**(1): p. 33-60.

30. Zhou, J., et al., *Synthesis of porous magnetic hollow silica nanospheres for nanomedicine application.* Journal of Physical Chemistry C, 2007. **111**(47): p. 17473-17477.

31. Dobson, J., *Magnetic nanoparticles for drug delivery.* Drug Development Research, 2006. **67**(1): p. 55-60.

32. Koh, I., et al., *Magnetic iron oxide nanoparticles for biorecognition: Evaluation of surface coverage and activity.* Journal of Physical Chemistry B, 2006. **110**(4): p. 1553-1558.

33. Yang, H.H., et al., *Magnetite-containing spherical silica nanoparticles for biocatalysis and bioseparations.* Analytical Chemistry, 2004. **76**(5): p. 1316-1321.

34. Blanco-Mantecon, M. and K. O'Grady, *Interaction and size effects in magnetic nanoparticles.* Journal of Magnetism and Magnetic Materials, 2006. **296**(2): p. 124-133.

35. Chan, C.K., et al., *High-performance lithium battery anodes using silicon nanowires.* Nature Nanotechnology, 2008. **3**(1): p. 31-35.

36. Liu, H.C. and S.K. Yen, *Characterization of electrolytic Co3O4 thin films as anodes for lithium-ion batteries.* Journal of Power Sources, 2007. **166**(2): p. 478-484.

37. Wang, L., et al., *Electrospinning synthesis of C/Fe3O4 composite nanofibers and their application for high performance lithium-ion batteries.* Journal of Power Sources, 2008. **183**(2): p. 717-723.

38. van de Krol, R., A. Goossens, and E.A. Meulenkamp, *In situ X-ray diffraction of lithium intercalation in nanostructured and thin film anatase TiO2.* Journal of the Electrochemical Society, 1999. **146**(9): p. 3150-3154.

39. Thackeray, M.M., W.I.F. David, and J.B. Goodenough, *Structural Characterization of the Lithiated Iron-Oxides Lixfe3o4 and Lixfe2o3 (0-Less-Than-X-Less-Than-2).* Materials Research Bulletin, 1982. **17**(6): p. 785-793.

40. Mitra, S., et al., *Growth and electrochemical characterization versus lithium of Fe3O4 electrodes made via electrodeposition.* Advanced Functional Materials, 2006. **16**(17): p. 2281-2287.

41. Taberna, L., et al., *High rate capabilities Fe3O4-based Cu nano-architectured electrodes for lithium-ion battery applications.* Nature Materials, 2006. **5**(7): p. 567-573.

42. Sivakumar, V., et al., *Magnetic and structural investigation of electrochemically lithiated magnetite nanoparticles.* Ieee Transactions on Magnetics, 2007. **43**(6): p. 3121-3123.

43. Ito, S., et al., *Lithium battery having a large capacity using Fe3O4 as a cathode material.* Journal of Power Sources, 2005. **146**(1-2): p. 319-322.

44. Komaba, S., T. Mikumo, and A. Ogata, *Electrochemical activity of nanocrystalline Fe3O4 in aprotic Li and Na salt electrolytes.* Electrochemistry Communications, 2008. **10**(9): p. 1276-1279.

45. Zhu, S.L., et al., *Crystallite Size Control and Resulting Electrochemistry of Magnetite, Fe3O4.* Electrochemical and Solid State Letters, 2009. **12**(4): p. A91-A94.

46. Zhang, W.M., et al., *Carbon Coated Fe3O4 Nanospindles as a Superior Anode Material for Lithium-Ion Batteries.* Advanced Functional Materials, 2008. **18**(24): p. 3941-3946.

47. Liu, H., et al., *Magnetite/carbon core-shell nanorods as anode materials for lithium-ion batteries.* Electrochemistry Communications, 2008. **10**(12): p. 1879-1882.

48. Guan, N.N., et al., *A simple one-pot synthesis of single-crystalline magnetite hollow spheres from a single iron precursor.* Nanotechnology, 2009. **20**(10).

49. Zhu, L.P., et al., *One-pot template-free synthesis of monodisperse and single-crystal magnetite hollow spheres by a simple solvothermal route.* Crystal Growth & Design, 2008. **8**(3): p. 957-963.

50. Hu, P., et al., *Fabrication of Monodisperse Magnetite Hollow Spheres.* Journal of Physical Chemistry C, 2009. **113**(3): p. 900-906.

51. Chen, X.Y., et al., *Hollow magnetite spheres: Synthesis, characterization, and magnetic properties.* Chemical Physics Letters, 2006. **422**(1-3): p. 294-298.

52. Maugis, D., *Adhesion of Spheres - the Jkr-Dmt Transition Using a Dugdale Model.* Journal of Colloid and Interface Science, 1992. **150**(1): p. 243-269.

53. Lin, D.C., E.K. Dimitriadis, and F. Horkay, *Elasticity of rubber-like materials measured by AFM nanoindentation.* Express Polymer Letters, 2007. **1**(9): p. 576-584.

54. Thackeray, M.M., *Spinel electrodes for lithium batteries.* Journal of the American Ceramic Society, 1999. **82**(12): p. 3347-3354.

55. Bard, A.J. and L.R. Faulkner, *Electrochemical Methods: Fundamentals and Applications.* 2001.

56. Li, W.Y., L.N. Xu, and J. Chen, *Co3O4 nanomaterials in lithium-ion batteries and gas sensors.* Advanced Functional Materials, 2005. **15**(5): p. 851-857.

57. Lee, K.T., Y.S. Jung, and S.M. Oh, *Synthesis of tin-encapsulated spherical hollow carbon for anode material in lithium secondary batteries.* Journal of the American Chemical Society, 2003. **125**(19): p. 5652-5653.

58. Mao, H.K., et al., *Isothermal Compression of Magnetite to 320 Kbar and Pressure-Induced Phase-Transformation.* Journal of Geophysical Research, 1974. **79**(8): p. 1165-1170.

59. Lou, X.W., et al., *Preparation of SnO2/Carbon Composite Hollow Spheres and Their Lithium Storage Properties.* Chemistry of Materials, 2008. **20**(20): p. 6562-6566.

60. Do, J.S. and C.H. Weng, *Preparation and characterization of CoO used as anodic material of lithium battery.* Journal of Power Sources, 2005. **146**(1-2): p. 482-486.

61. Lou, X.W., C.M. Li, and L.A. Archer, *Designed Synthesis of Coaxial SnO2@carbon Hollow Nanospheres for Highly Reversible Lithium Storage.* Advanced Materials, 2009. **21**(19): p. NA.